

# A birdcage resonant antenna for helicon wave generation in TORPEX

Simon Vincent, Philippe Guittienne, Patrick Quigley, Cyrille Sepulchre, Rémy Jacquier, Robert Bertizzolo, Marcelo Baquero-Ruiz, Alan A. Howling, and Ivo Furno  
*École Polytechnique Fédérale de Lausanne (EPFL), Swiss Plasma Center (SPC), CH-1015 Lausanne, Switzerland*

(Dated: 9 April 2024)

A birdcage resonant helicon antenna is designed, mounted and tested in the toroidal device TORPEX. The birdcage resonant antenna is an alternative to the usual Boswell or half-helical antenna designs commonly used for  $\sim 10$  cm diameter helicon sources in low temperature plasma devices. The main advantage of the birdcage antenna lies in its resonant nature, which makes it easily operational even at large scales, an appealing feature for the TORPEX device whose poloidal cross section is 40 cm in diameter. With this antenna helicon waves are shown to be launched and sustained throughout the whole torus of TORPEX. The helicon waves can be launched at low power on a pre-existing magnetron-generated plasma with little effect on the density profiles. The birdcage antenna can also be used alone to produce plasma, which removes the constraint of a narrow range of applied magnetic fields required by the magnetron, opening the way to a new range of studies on TORPEX with the external magnetic field as a control parameter.

PACS numbers: Valid PACS appear here

## I. INTRODUCTION

Helicon waves are bounded whistler waves, belonging to the right hand polarized part of electromagnetic waves that can propagate in magnetized plasmas, at frequencies between the ion and electron cyclotron frequencies  $\omega_{ci} \ll \omega \ll \omega_{ce}$ . Helicon waves have attracted a lot of interest from the 1970s in the context of low-temperature plasmas, as they were found to have a surprisingly high ionization efficiency<sup>1</sup>: for sufficient input power the energy transfer from the wave to the plasma abruptly increases, reaching the so-called "helicon mode"<sup>2</sup>. Since then, a lot of experimental and theoretical studies have been carried out to better understand helicon properties and energy transfer capabilities. The higher ionization efficiency of helicon sources over the conventional ICP (inductively coupled plasma) sources, in configurations comprising an external magnetic field, is still a subject of active research. In the meantime, helicon sources have been developed across the globe and are now routinely used for plasma generation in laboratory devices<sup>3-7</sup>, as well as in industry<sup>2</sup>. Low-temperature plasma helicon sources can also be used for wall conditioning in tokamaks<sup>8</sup>. In the context of fusion, helicon waves have also been considered as a promising candidate for current drive in tokamaks<sup>9,10</sup>. A number of numerical simulations of helicon wave propagation and absorption efficiency were performed in fusion relevant conditions<sup>11-13</sup> to predict the performances of helicon current drive as well as for antenna design purposes. A recently mounted planar helicon antenna is currently being tested on the DIII-D tokamak<sup>14</sup>, another one has been mounted on the tokamak KSTAR<sup>15</sup>. Experimental investigations of helicon wave physics in a toroidal geometry can nevertheless greatly benefit from fundamental studies in low temperature basic plasma devices, which can be performed in very well diagnosed systems at a lower cost.

Helicon sources have been installed in a few low temperature plasma toroidal devices<sup>16-18</sup> and stellarator<sup>19</sup>, but few studies focused on the helicon waves themselves. Refs.<sup>19-21</sup> provide an interesting set of helicon wave amplitude mea-

surements in toroidal configurations, in devices with major radii  $\lesssim 30$  cm. Nonetheless, experimental studies of helicon waves have been mostly restricted to cylindrical devices. To the knowledge of the authors, little is known about the effect of a toroidal geometry on the fundamental properties of helicon waves. To bridge this gap, we have designed and installed a helicon source in TORPEX<sup>22</sup>, a toroidal device of major radius 1 m and minor radius 20 cm.

In all previous studies, TORPEX relied on microwaves, generated by a magnetron, to create and sustain a plasma. To this end the magnetron frequency has to match the electron cyclotron frequency  $\omega_{ce}$  or lower hybrid frequency  $(\omega_{ce}^2 + \omega_{pe}^2)^{1/2}$  (see Ref.<sup>23</sup>), which restricted the studies in TORPEX to values of the total magnetic field  $B \in [650; 850]$  G. This further motivated the helicon antenna, whose operation enables experiments in a very wide range of values of  $B$ , hence opening the possibility for a whole new range of studies in TORPEX with  $B$  as a control parameter.

This article presents the installation and first results of the newly mounted helicon source in TORPEX. The device TORPEX is presented in Sec. II along with the diagnostics used in the present work. The antenna design that is chosen is that of a birdcage resonant helicon antenna, or birdcage antenna (BCA). The BCA is then introduced in Sec. III, together with a thorough explanation of the advantages provided by this design. In Sec. IV, the successful propagation of helicon waves launched by the BCA in TORPEX is demonstrated. Section V finally presents a series of measurements establishing the BCA ability to sustain plasma in various conditions. Conclusions are finally given in Sec. VI.

## II. TORPEX DEVICE AND DIAGNOSTICS

TORPEX is a toroidal device of major and minor radii 1 m and 20 cm respectively (Fig. 1). We use here a simple toroidal coordinate system  $(\hat{r}, \hat{\phi}, \hat{z})$  as shown in Fig. 1, with the origin  $(0, 0, 0)$  taken at the center of the BCA. The stainless steel

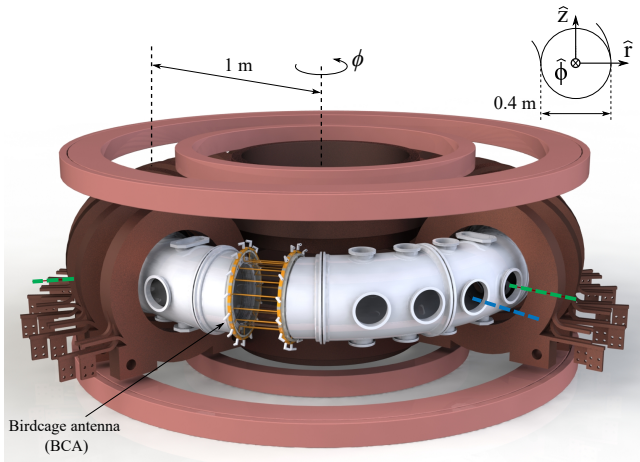


FIG. 1. TORPEX device, with the BCA. The Langmuir probe (blue dashed line) is inserted at the toroidal location  $\phi \approx +80^\circ$ , and the B-dot probes (green dashed lines) at the locations  $\phi \approx -80^\circ$  and  $\phi \approx +100^\circ$ , on the left or right sides of the antenna respectively. Note that toroidal coils on TORPEX surround the whole chamber: a set of these coils are not shown in the figure for a better visualisation of the chamber.

chamber of TORPEX is surrounded by a set of 28 toroidal coils and 5 pairs of poloidal coils, enabling a wide variety of magnetic configurations, with values of the total magnetic field potentially up to 1000 G. The magnetic configuration chosen for this study is the so-called Simple Magnetized Torus (SMT)<sup>24,25</sup> that consists of a dominant toroidal field with a smaller vertical field, of values  $B_{tor} \approx 780$  G and  $B_{ver} \approx 20$  G respectively (averaged over the poloidal cross section). Hydrogen or argon plasmas can be generated by a 2.45 GHz magnetron, upon injection of the corresponding gases into the vessel to a pressure of  $\sim 10^{-4}$  mbar up to  $\sim 10^{-3}$  mbar. The main vessel of TORPEX is composed of 8 toroidal sectors. One of these sectors was replaced by two flanges and a borosilicate tube surrounded by a BCA, whose technical details and capabilities are the subject of Sec. III.

The plasma density  $n_e$  and floating potential  $V_f$  are measured with a Langmuir probe, scanning radial positions at  $z = 0$  cm and at a toroidal angle  $\phi \approx +80^\circ$  away from the antenna center (see blue dashed line in Fig. 1). The density is obtained from measurements of the ion saturation current  $I_{i,sat}$ , that is collected with a probe tip biased at  $V_{bias} = -60$  V. We then use  $n_e = |I_{i,sat}| / (\alpha_0 e A \sqrt{e T_e / m_i} \beta)$ , with  $\alpha_0 = 0.5$  a coefficient taking into account the effect of the pre-sheath<sup>26,27</sup>,  $e$  the electron charge,  $A$  the probe tip surface,  $T_e$  the electron temperature assumed here constant at 4 eV (measurements in similar conditions show  $T_e \sim 2 - 5$  eV),  $m_i$  the ion mass, and  $\beta = (1 - \gamma(V_{bias} - V_f))$  a coefficient accounting for the sheath expansion. Based on results from previous studies<sup>28</sup>, we use here  $\gamma \sim 0.05$ .

A magnetic probe (dubbed B-dot probe) is used to measure the magnetic field fluctuations along all axes ( $\hat{r}, \hat{\phi}, \hat{z}$ ) at any selected location. The B-dot probe consists of three orthogonal 5 mm  $\times$  5 mm square coils, each made of 10 loops

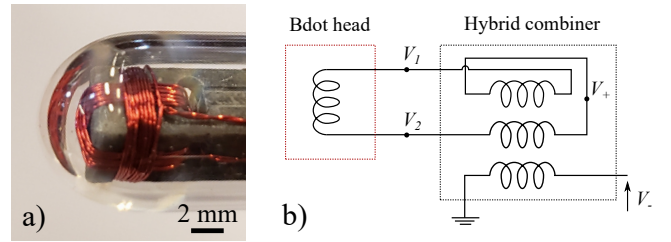


FIG. 2. a) B-dot probe head. b) Electrical sketch of one of the coils of the B-dot, with a hybrid combiner measuring  $V^- = (V_1 - V_2)/2$ , leaving the B-dot head electrically floating in the plasma.

of 0.2 mm coated copper wire. The probe's head is mounted on a ceramic tube and inserted in a closed-end glass tube to provide protection from direct contact with the plasma. The coil ends are connected from the probe's head to hybrid combiners, from which the B-dot measurement is acquired. Note that the connections from the 6 ends of the probe's head to the hybrid combiners are done with individual coaxial cables, which protects the measurement from capacitive or inductive pick-up along this transmission line.

A picture of the probe's head with the coils is shown in Fig. 2 (a) and the circuit diagram corresponding to each coil is drawn in Fig. 2 (b). As shown in Fig. 2 (b) each one of the three B-dot coils (with given potentials  $V_1$  and  $V_2$  at its ends) is connected to a hybrid combiner, composed of three coils wound together, hence providing the measurement of  $V^- = (V_1 - V_2)/2$ . This way the induced current in the coil is directly obtained, removing the potential capacitive pick-up from the plasma (that would affect in the same way  $V_1$  and  $V_2$ ). In addition using hybrid combiners enables the B-dot coils to be electrically floating and unperturbed by the acquisition system.

B-dot measurements were performed along  $r$  and at  $z = 0$  cm, at the toroidal angles  $\phi \approx -80^\circ$  and  $\phi \approx +100^\circ$  away from the antenna center, as shown in green dashed lines in Fig. 1. More details on the B-dot probe calibration are provided in appendix A. As will be presented in section IV, B-dot measurements reveal the presence of helicon waves generated by the BCA.

### III. THE BIRDCAGE RESONANT HELICON ANTENNA

Since the discovery of the high ionization efficiency of helicon sources, numerous designs have been developed. Among these are the well known Boswell antenna<sup>1</sup>, or the half helical antenna<sup>29</sup> that is now the most commonly used one in linear devices, where the antenna diameters are typically  $d \lesssim 10$  cm. All these designs essentially consist of wire loops, which are inductive elements. Even when coupled to the generated plasma, whose impedance is partly resistive due to collisions, these helicon plasma sources have an impedance that is mostly inductive. When fed by a RF power supply, the antenna input is therefore prone to high voltages. This can lead to arcing problems, making plasma generation difficult to achieve when the size of the antenna is increased. It is however worth men-

tioning here the work of Ref.<sup>30</sup> where a very large half helical antenna of 44 cm diameter could be used for plasma generation, and even reach helicon mode coupling as reported by the authors. The RF engineering difficulties that had to be overcome to get these results are not detailed in the article.

In the case of TORPEX, we chose an alternative helicon antenna design, the BCA, which advantages are explained in Sec. III A. The choice of the specific BCA design to be mounted on TORPEX is then motivated by COMSOL simulations in Subsec. III B. The final design and installation of the BCA on TORPEX is presented in Subsec. III C.

### A. Description and advantages of the BCA

The key feature of a BCA is that it is a resonant device. This type of antenna consists of an assembly of legs of inductance  $L$  connected in parallel by capacitors of capacitance  $C$ , as shown in Fig. 3 (a). This circuit has resonance frequencies  $\omega_{res}^p \sim 1/\sqrt{2LC \sin^2(\frac{p\pi}{2N})}$  (see Ref.<sup>31</sup>) with  $N$  the number of inductive legs and  $p \in [1; N-1]$ .

At resonance, the input impedance  $Z$  of such a circuit becomes mostly real, which is a major difference compared to the classical helicon antennae mentioned before. When the excitation frequency matches a resonance frequency, the real part of the impedance  $\text{Re}(Z)$  typically reaches a value of the order of a few hundred Ohm (when coupled to plasma  $\text{Re}(Z)$  is even further reduced to few tens of Ohm), and the imaginary part  $\text{Im}(Z)$  is small (a few Ohm) to negligible. Therefore the phase shift between the input voltage  $U_{in}$  and current  $I_{in}$  is close to zero, and the input power that is dissipated by the antenna does not require high voltages nor high currents. Such an antenna is therefore scalable to larger dimensions than ICP or conventional helicon sources, while avoiding arcing problems. As an example, with an ICP made of a 4 turns solenoid with diameter 13 cm, and powered by a 1 kW, we can expect  $U_{in} \approx 9500$  V and  $I_{in} \approx 30$  A. With a BCA of diameter 13 cm and same input power, we only have  $U_{in} \approx 140$  V and  $I_{in} \approx 7$  A (see Ref.<sup>32</sup>).

Being bound to operate at resonance can be seen as a significant inconvenience of this antenna design. In reality this aspect is not too restricting, because the BCA operation is in fact quite robust: even if the power supply frequency does not perfectly match the targeted resonance, we still have  $\text{Re}(Z) \sim \text{Im}(Z)$ . This is enough to substantially reduce the voltage levels compared to a situation where  $\text{Re}(Z) \ll \text{Im}(Z)$ , and hence scale up the antenna.

To make a BCA, the planar circuit sketched in Fig. 3 (a) is rolled in a cylindrical shape as shown in Fig. 3 (c). The connection to the ground is made at the location opposite to the RF input (details on the reason for this choice can be found in Ref.<sup>31</sup>). On the other side of this ground connection, along the cylinder axis, the circuit is left open. Selecting the resonance frequency corresponding to  $p = 2$  results in a current distribution in the legs which follows a sinusoidal pattern, corresponding to an azimuthal mode  $m = 1$ . Note that in the following,  $m$  refers to the poloidal wavenumber of a helicon wave of the

form  $e^{i(\omega t - m\theta - k_\phi \phi)}$ , with  $\theta = \sqrt{r^2 + z^2}$  the poloidal angle and  $k_\phi$  the toroidal wavenumber. Arranged in a cylindrical shape, the legs then produce an homogeneous transverse magnetic field, that is able to excite helicon waves (see Fig. 3 (b) and (c)).

An additional advantage of the BCA is that such a sinusoidal pattern is well suited for the exclusive excitation of the helicon modes  $|m| = 1$ . Indeed, a half-helical antenna having only 2 legs (whose current amplitudes would be the maxima in Fig. 3 (b)) is able to excite all modes  $m = 2q$ , with  $q \in \mathbb{Z}$ . Thus, the power this antenna transfers to the plasma is likely to be scattered among various modes  $m$ . In contrast to this, the BCA benefits from a more targeted coupling to the modes  $|m| = 1$ , and avoids this spread in energy transfer, by imposing with  $N$  points an azimuthal wavelength corresponding to modes  $|m| = 1$ . This is an appealing feature of the BCA excitation, since the helicon mode  $m = +1$  is known to be the most efficient for plasma ionization<sup>2</sup>.

The geometry of the BCA, with its legs wrapped around a cylinder, ensures moreover an important surface of interaction between the antenna currents and the plasma. The induction mode of a BCA is therefore easily achieved, even at low pressures compared to classical helicon antennae.

Another advantage is that the impedance characteristics of the BCA ( $\text{Re}(Z) \sim 100 \Omega$  and  $\text{Im}(Z) \lesssim \text{Re}(Z)$ ) make it easier to be matched to  $50 \Omega$ . This leads to lower levels of currents and less power dissipation in the matching-box (which is the intermediate element composed of variable capacitors placed between the RF power supply and the antenna, with which the matching is achieved). This also means that the coaxial cable connecting the matching-box to the BCA has to withstand a lower value of reflected power and is therefore less subjected to power dissipation and heating. This results in a better antenna efficiency, and makes in addition the antenna system easier to build and more practical to operate.

The main advantages of a BCA over the classical helicon antenna designs can be summarized as follows:

- Low input voltages and currents resulting from the resonant nature of the antenna, making it easily scalable to large dimensions.
- Sinusoidal distribution of currents in the legs, providing a better targeted energy deposition to helicon modes  $|m| = 1$ .
- Efficient inductive coupling and easy plasma ignition, thanks to the large surface covering of the high RF energy stored in the legs.
- Low power dissipation in the matching-box and input cable.

We note that these advantages come, of course, at the expense of a more complex design. A more detailed comparison between a BCA and a half-helical antenna in a simple linear device will be the subject of a forthcoming publication. For an in-depth description of the physics and engineering of the BCA, we refer the reader to Ref.<sup>32</sup>.

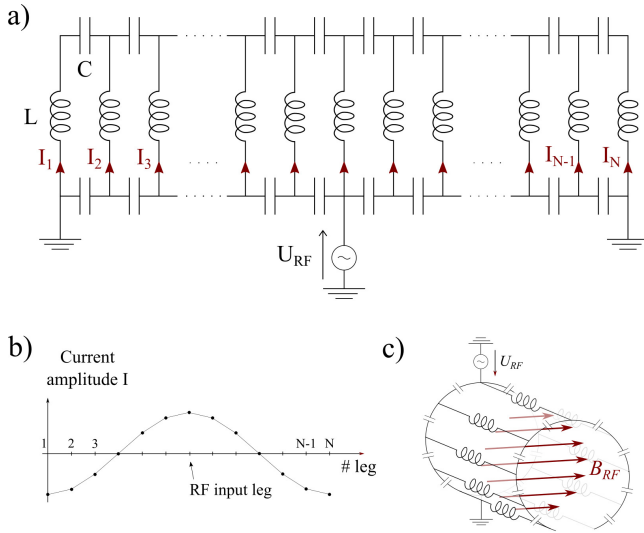


FIG. 3. a) Electrical circuit of the birdcage antenna resonant network. b) Sinusoidal distribution of currents amplitudes in the legs of a BCA, when excited at the resonance frequency corresponding to modes  $|m| = 1$ . c) Drawing of the resonant network folded around to form a birdcage antenna, with the transverse magnetic field induced at the resonance corresponding to  $|m| = 1$ .

## B. Numerical simulations

The installation of the BCA in TORPEX is done with a cylindrical glass tube of diameter 30 cm, connected to the toroidal vessel via two flanges that were designed to adapt the straight cylinder to the toroidal geometry of TORPEX. The geometry of the BCA is constrained on the inner side by the glass tube, and on the outer side by the toroidal coils of inner diameter 52 cm. With these spatial constraints, the value of the capacitances  $C$  of the antenna, as well as the length and shape of the legs (defining the value of  $L$ ), have to be chosen for the  $|m| = 1$  resonance to match the 13.56 MHz frequency of our power supply. We note in addition that the resonance frequency is expected to shift upwards in the presence of the plasma. To choose the best antenna shape and components, taking into account the spatial constraints and this frequency shift, numerical simulations with various BCA designs were performed with COMSOL®<sup>33</sup>.

The spatial domain for the simulations is a cylinder of diameter 80 cm and length 50 cm, that includes a plasma domain consisting of a cylinder of diameter 30 cm. These domains are shown in Fig. 4, together with the BCA design that was finally chosen, and that will be discussed in detail in Sec. III C. The BCA is placed around the plasma domain, with the legs at 1.5 cm from the plasma (hence from the inner tube boundary). The capacitors are treated as lumped elements, while the boundaries of the legs and the outer limits of the vacuum domain are perfectly conducting surfaces such that  $\vec{n} \times \vec{E} = \vec{0}$ , where  $\vec{n}$  is the unity vector perpendicular to the surface and  $\vec{E}$  the electric field at the surface. An external magnetic field  $B_0$  is imposed along the axial direction of the cylindrical domain as shown in Fig. 4. The plasma is treated as a dielectric, and

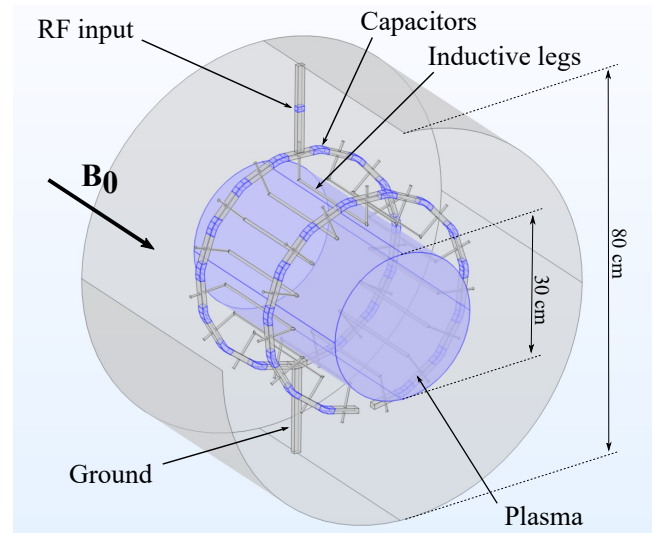


FIG. 4. Geometry of the birdcage antenna and spatial domain of the COMSOL numerical simulations.

the electromagnetic field is modeled with

$$\vec{\nabla} \times (\vec{\nabla} \times \vec{E}) - k_0^2 \left( \mathbf{I} - \frac{i}{\omega \epsilon_0} \boldsymbol{\sigma} \right) \cdot \vec{E} = \vec{0},$$

with a conductivity  $\boldsymbol{\sigma} = \mathbf{0}$  in vacuum, and in the plasma:

$$\boldsymbol{\sigma} = \alpha \begin{pmatrix} \gamma^2 & \gamma \omega_{ce} & 0 \\ -\gamma \omega_{ce} & \gamma^2 & 0 \\ 0 & 0 & \gamma^2 + \omega_{ce}^2 \end{pmatrix} \quad \text{and} \quad \begin{cases} \alpha & = \frac{\epsilon_0 \omega_p^2}{\gamma(\gamma^2 + \omega_{ce}^2)} \\ \gamma & = \nu + i\omega \end{cases}$$

with  $k_0 = c/\omega$ ,  $c$  the speed of light,  $\epsilon_0$  the vacuum permittivity,  $\omega_p = \sqrt{n_e e^2 / \epsilon_0 m_e}$  the plasma frequency,  $n_e$  the plasma density,  $e$  the electron mass,  $m_e$  the electron mass,  $\nu$  the electron neutral collision frequency. Here the neutral pressure is set at  $10^{-4}$  mbar, and we take  $\nu = n_n \sigma_{en} v_{th,e}$ , with  $n_n$  the neutral pressure,  $v_{th,e}$  the electron thermal velocity, and  $\sigma_{en} = 10^{-19} \text{ m}^2$  the electron neutral elastic collision cross section of hydrogen, taken from the LXCat database<sup>34,35</sup>, and evaluated at  $T_e \sim 5 \text{ eV}$ .

The plasma density is assumed to be uniform with  $n_e = 5 \times 10^{16} \text{ m}^{-3}$ , that is of the order of the maximal density expected on TORPEX at this pressure and for a power up to 1 kW. The high density taken here, for TORPEX standards, as well as taking a uniform profile, is a way of assessing the most unfavorable scenario for the antenna being impacted by the presence of the plasma. This allows us to estimate an upper limit for the frequency shift due to the plasma.

By performing series of simulations with a RF input frequency ranging from 5 to 17 MHz, the input impedance spectrum of the BCA can be obtained, showing various resonances corresponding to exciting modes  $m = 2n + 1$  with  $n \in \mathbf{N}$ . Figure 5 (a) shows the modulus of the BCA input impedance, for capacitances  $C = 2000 \text{ pF}$  and a simple design of the antenna with straight legs connecting the capacitors (red solid line). Figures 5 (b), (c) and (d) show the amplitude of the RF magnetic field generated by the BCA at frequencies corresponding

to resonances  $m = 1$ ,  $m = 3$  and  $m = 5$ , in a plane transverse to the BCA and at its center. As shown in Fig. 5 (a), when the value of the capacitance is lowered to 1000 pF (blue line) or increased to 3000 pF (yellow line) the whole spectrum is respectively shifted upwards or downwards in frequency; the resonances follow a trend  $\sim 1/\sqrt{LC}$ . The value of the capacitance can hence be finely tuned to choose the resonance frequency.

However the COMSOL simulations performed with and without plasma, showed that the simple design of a BCA with straight legs led to a substantial upward shift of the resonance frequencies, shift that would in addition strongly depend on  $B_0$  (with a shift of  $\approx 2$  MHz with  $B_0 = 0$  G, to  $\approx 0.1$  MHz with  $B_0 = 500$  G). This was considered to be impractical for studies on TORPEX that would imply varying  $B_0$ . This effect of frequency shift in presence of the plasma can be reduced. To do so we limit the part of the BCA legs that are close and hence coupled to the plasma, with respect to the total length of the legs. This is done by adding extensions to the legs, away from the antenna center. With straight leg extension as shown in Fig. 4 for instance, only  $\approx 2/3$  of the legs are coupled to the plasma. This significantly reduces the resonance frequency shift to  $\approx 0.3 - 0.7$  MHz for  $B_0 \in [0; 500]$  G. Note that of course by changing the leg total length, the value of  $L$  is increased, leading to a change in the BCA spectrum as shown in Fig. 5 (a) (dashed and dotted red curves). The leg design has therefore to be chosen first, and the value of the capacitance is then adjusted to choose the  $m = 1$  resonance frequency at  $\approx 13.56$  MHz in the presence of plasma.

Overall various BCA designs have been explored, and a large number of simulations were performed, that will not be discussed in detail here. Although the frequency shift could be reduced even more, with longer leg extensions in the shape of helices for example (see red dotted curve in Fig. 5 (a)), the final design is the one sketched in Fig. 4, that combines a good reduction of the resonance frequency shift with a relative simplicity of the design. The BCA characteristics are detailed in subsection III C.

### C. Final design of the BCA and preliminary tests

The final design of the BCA and its installation in TORPEX are presented in Fig. 6. The capacitances  $C$  correspond to assemblies of four capacitors in parallel (Fig. 6 (b)), two of 430 pF and two of 470 pF adding up to a total capacitance of 1800 pF. Each capacitor can withstand up to 15 A rms without the need for active cooling: the assemblies can then support up to 60 A rms, corresponding to an input antenna power of up to a few kW in continuous mode. Without cooling of the capacitors, higher power can still be tested in pulse mode. The legs are L-shaped (Fig. 6 (c)) and connected at their ends to the capacitor assemblies via brass pieces (Fig. 6 (e), (f)).

The BCA is supported by circular 3D printed pieces that are attached to the flanges on both sides (Fig. 6 (c)). Note that the spacing between the glass tube and the side flanges is smaller on the high field side than on the low field side (Fig. 6 (a)), which ensures that the center of the BCA overlaps

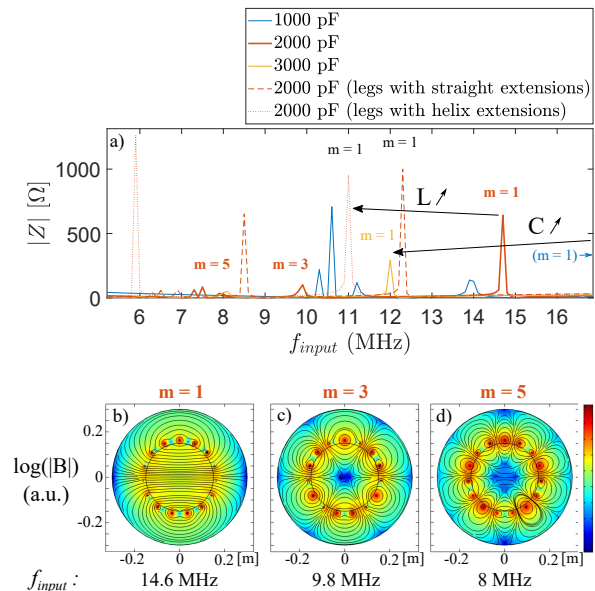


FIG. 5. a) Input impedance spectrum of the birdcage resonant antenna, for values of the capacitance  $C \in [1000, 2000, 3000]$  pF and three designs of the inductive legs: simple legs without extension, legs with straight extensions (see Fig. 4), and legs with helix extensions. b-c-d) Amplitude of the RF magnetic field simulated for an excitation frequency of the antenna corresponding respectively to modes  $m = 1$ ,  $m = 3$  and  $m = 5$ .

the main vessel toroidal central axis  $\phi$ . A matching-box of type T was built to connect the RF power supply to the BCA. This matching-box is composed of two sets of a 0 – 500 pF variable capacitor and 2.3  $\mu$ H in-house made coils connected in series, with a 100 pF capacitor in between and connected to the ground (see Ref.<sup>32</sup> for more details on type T matching-box).

The BCA was first mounted on a testbench composed of the glass tube and two flanges. The measured input impedance (real and imaginary parts) of the antenna is shown in Fig. 7 (a). The clearly visible five largest peaks correspond to excitation modes  $m = \{1, 3, 5, 7, 9\}$  of the RF transverse magnetic at corresponding frequencies  $f = \{13.2, 8.7, 6.9, 6.5, 6.3\}$  MHz, with a highest resonance impedance for  $m = 1$  at  $|Z| \approx \Re(Z) \approx 380 \Omega$ .

After initial tests, the antenna was mounted on TORPEX, and the measured input impedance is shown in Fig. 7 (b). The resonance frequency of mode  $m = 1$  is shifted down to 12.45 MHz, with a corresponding resistive impedance peaking at 710  $\Omega$ . This downward shift of the spectrum is expected to be due to the close proximity to the magnetic field coils, the vacuum vessel, and other conducting materials. To study the impact of the plasma on the impedance, argon plasma is generated with the magnetron at power 600 W, and with an external field of  $B_{tor} \approx 780$  G. As shown in the next subsection this plasma reaches a density of  $\sim 10^{16} \text{ m}^{-3}$  and is localized near the high field side around  $-12 \leq r \leq -2$ . Figure 7 (b) shows that in the presence of plasma the resonance frequency is slightly shifted upwards to 12.7 MHz. The peak of  $\Re(Z)$

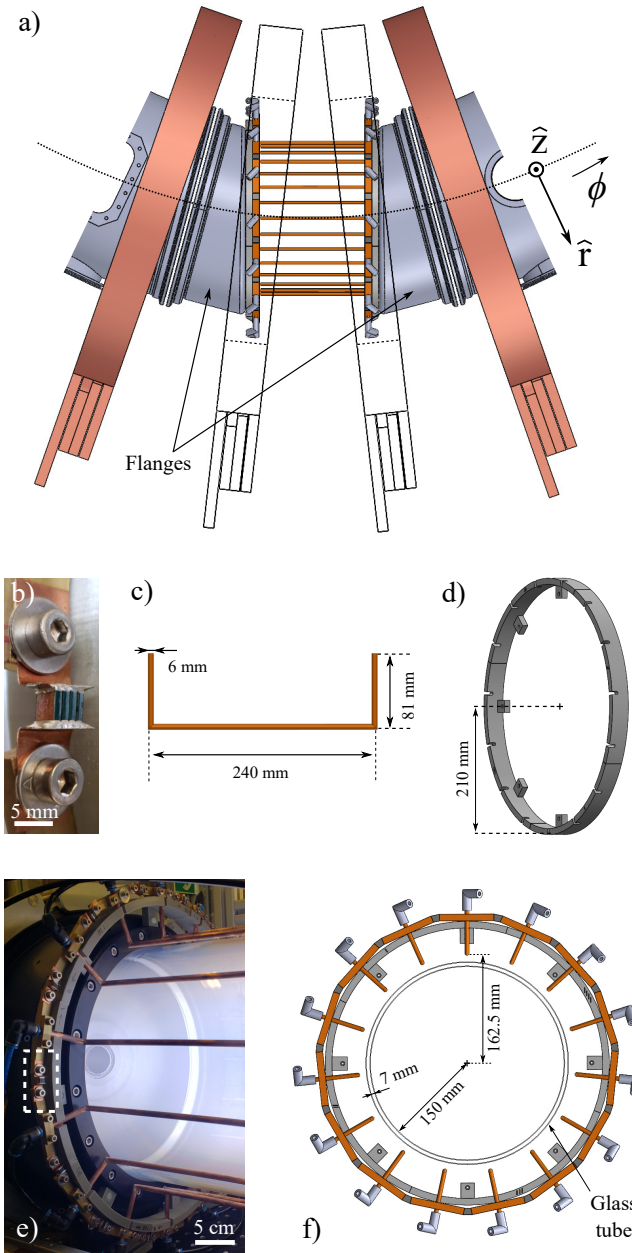


FIG. 6. Elements of the BCA mounted on TORPEX. See text for details.

is enlarged and its maximum value reduced to  $200 \Omega$ .

With the strong impact of TORPEX environment surrounding elements, and even with the upward frequency shift due to the presence of the plasma, the resonance frequency is then  $\approx 1$  MHz lower than the frequency originally planned of 13.56 MHz that is set by the RF power supply. The capacitor assemblies could be changed to correct this, but as will be seen in section IV such a change is not necessary for the correct operation of the BCA. At 13.56 MHz we have in the presence of plasma  $\text{Re}(Z) \approx 20 \Omega$  and  $\text{Im}(Z) \approx 30 \Omega$ . In these conditions the matching of this input impedance to  $50 \Omega$  is easily achieved, and draws low currents in the matching-box

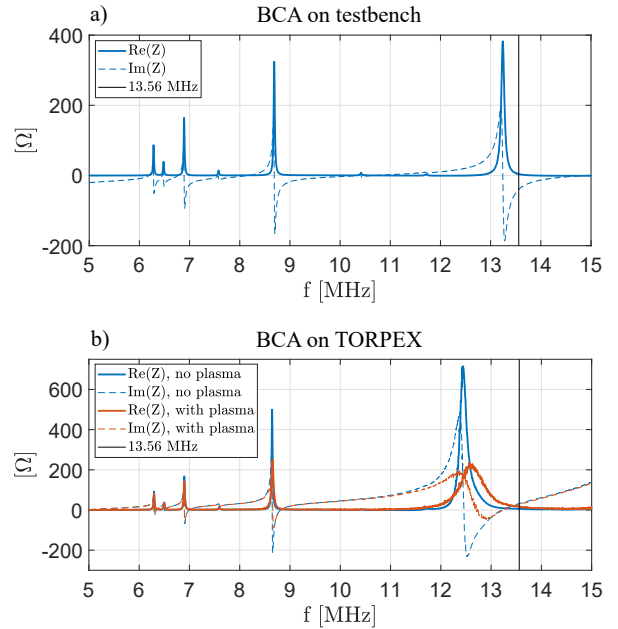


FIG. 7. Input impedance of the BCA, measured on a testbench (a) and when mounted on TORPEX (b) with and without a background magnetron plasma.

and in the cable connecting the matching-box to the BCA. The connection cable does not require water cooling, which simplifies the mounting of the BCA in TORPEX. Once the BCA mounted, its ability to launch and sustain helicon waves, as well as to generate plasma in TORPEX, is explored.

#### IV. PROPAGATION OF TOROIDAL HELICON WAVES

First measurements of helicon waves excited by the BCA in TORPEX are now presented, in magnetron-generated hydrogen plasmas at a pressure of  $\sim 10^{-4}$  mbar. The magnetic configuration is the SMT configuration introduced in Sec. II. The magnetron power is set at  $P_{MAG} = 600$  W, and the BCA is fed with an RF power of  $P_{BC} = 200$  W.

Before looking at the excited helicon waves, we look at the impact of the BCA on the background plasma parameters. Radial profiles of the density  $n_e$  and floating potential  $V_f$  measured with a Langmuir probe are shown in Fig. 8 (a) and (b) respectively, both with the BCA powered off (blue curves) and on (red curves). The error bars in shaded regions are the root-mean-square of the measured fluctuations. The bulk of the magnetron generated plasma is located in the region  $-12 \leq r \leq 6$  cm, with  $n_e \approx 8 \times 10^{16} \text{ m}^{-3}$  around  $r = -2$  cm. This density profile is not modified by the BCA powered at 200 W. The floating potential however, whose absolute value remains low across the profile with  $|V_f| \lesssim 2$  V with the magnetron plasma, is lowered around  $r \approx \pm 10$  cm when the bird-cage is on, reaching  $V_f \approx -6$  V. Note that this happens close to the glass tube boundary, at  $r = \pm 15$  cm, and might indicate an electron temperature increase near the BCA. The effect of the BCA upon  $n_e$  and  $V_f$  depending on the control parameters

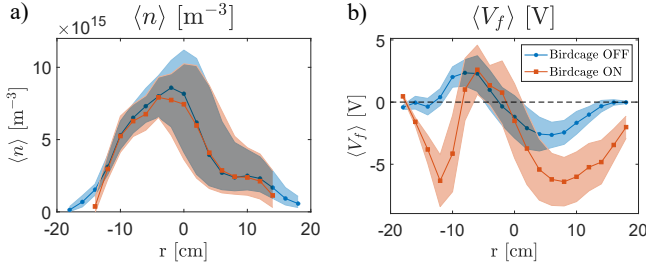


FIG. 8. Radial profiles of the density (a) and floating potential (b) measured by Langmuir probe at  $z = 0$  cm, for  $P_{MAG} = 600$  W. The blue curves are measurements with the birdcage antenna off, the red curves with  $P_{BC} = 200$  W.

are discussed in more detail in Sec. V.

Fluctuations of the magnetic field in the 3 directions ( $\tilde{B}_r, \tilde{B}_\phi, \tilde{B}_z$ ) are measured with the B-dot probe. An example is shown in Fig. 9, where each measurement is acquired over 1 ms, at a sample frequency of 500 MHz. The raw signals are filtered around  $f_0 = 13.56$  MHz (Fig. 9 (b)), and converted to mG (Fig. 9 (a)) with the calibration procedure detailed in appendix A. With the magnetron alone, the measured fluctuations of  $B$  are below  $\sim 0.3$  mG, which can be considered as the noise level of the B-dot measurements. When the BCA is powered,  $B$  fluctuations of the order 10 mG are measured on both sides of the BCA, indicating that the BCA is indeed able to excite and launch electromagnetic waves in the plasma. In the magnetic configurations studied here, large-amplitude low frequency fluctuations are observed (see example of Fig. 9 (a)). The time evolution of the helicon waves is however very stable on the time scale of a few tens of 13.56 MHz periods (Fig. 9 (c)).

The local polarization as well as the poloidal shape of the helicon wave is obtained by looking at the temporal evolution of  $(\tilde{B}_r, \tilde{B}_z)$ , as shown in (Fig. 9 (d)). We observe an elliptical polarization of the waves, which is a characteristic of helicon waves. In argon and with an external magnetic field of  $\approx 780$  G we have  $\omega_{ci} \approx 10^5$  Hz and  $\omega_{ce} \approx 10^{10}$  Hz. In hydrogen  $\omega_{ci} \approx 7 \times 10^6$  Hz. We can therefore conclude that the measured waves propagating in TORPEX at a frequency of 13.56 MHz ( $\omega = 8.52 \times 10^7$  Hz), that fall in the range  $\omega_{ci} \ll \omega \ll \omega_{ce}$ , are indeed helicon waves.

Radial scans are performed with the B-dot probe along  $r \in [-18; 18]$  cm by steps of 3 cm, at  $z = 0$  cm, and both on the left and right sides of the BCA at the toroidal locations  $\phi \approx -80^\circ$  and  $\phi \approx +100^\circ$ , corresponding respectively to the toroidal distances of  $\approx -1.4$  m (left) and  $\approx +1.8$  m (right) away from the BCA center. The amplitudes of the magnetic field fluctuation components ( $|\tilde{B}_r|, |\tilde{B}_\phi|, |\tilde{B}_z|$ ) are then computed as the average amplitude over 10 periods. The time evolution of these averaged amplitudes is shown in Fig. 10, with the standard deviation of their fluctuations displayed as shaded areas. Figure 10 (a) and (b) are measurements performed respectively left and right of the BCA. The radial component  $\tilde{B}_r$  is the strongest overall, which is expected as it corresponds to the direction of the magnetic field excited by the BCA (see Fig. 4 (b)). The shape of  $|\tilde{B}_r|$  is centred and al-

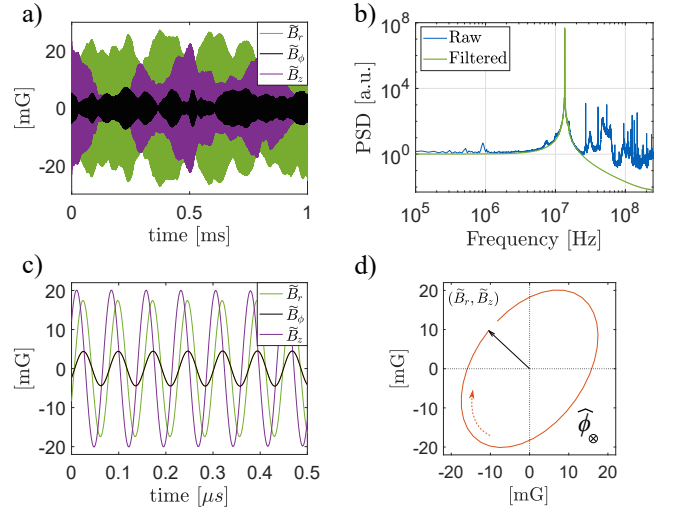


FIG. 9. a, c) Time evolution of  $(\tilde{B}_r, \tilde{B}_\phi, \tilde{B}_z)$  measured by B-dot probe at  $(r, \phi, z) = (0, +100^\circ, 0)$ . b) Raw and filtered spectra of  $\tilde{B}_r$ . d) Time evolution of  $(\tilde{B}_r, \tilde{B}_z)$  over one period, showing the polarization of the helicon wave.

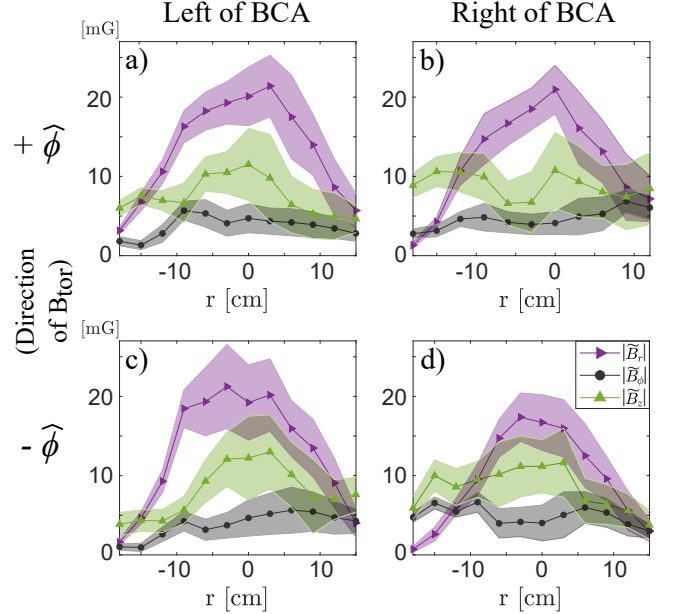


FIG. 10. Amplitude of the magnetic field fluctuations measured by the B-dot probe, as a function of the radius, at  $z = 0$  cm. The measurements are performed at the left (a,c) or right (b,d) of the antenna, as seen from the top, and with the toroidal field  $B_{tor}$  along  $+\hat{\phi}$  (a,b) or  $-\hat{\phi}$  (c,d).

most symmetric around  $r = 0$  cm; interestingly this does not follow the amplitude of the density, that is off-centred around  $r \sim -4$  cm as seen in Fig. 8 (a). Note also an increase from the high field side to the low field side of both the radial and toroidal components  $\tilde{B}_r$  and  $\tilde{B}_\phi$ , that is likely to be due to the toroidicity of the wave propagation. This is still to be further investigated in future studies.

Figures 11 (a) and (b) show the time evolution of  $(\tilde{B}_r, \tilde{B}_z)$ ,

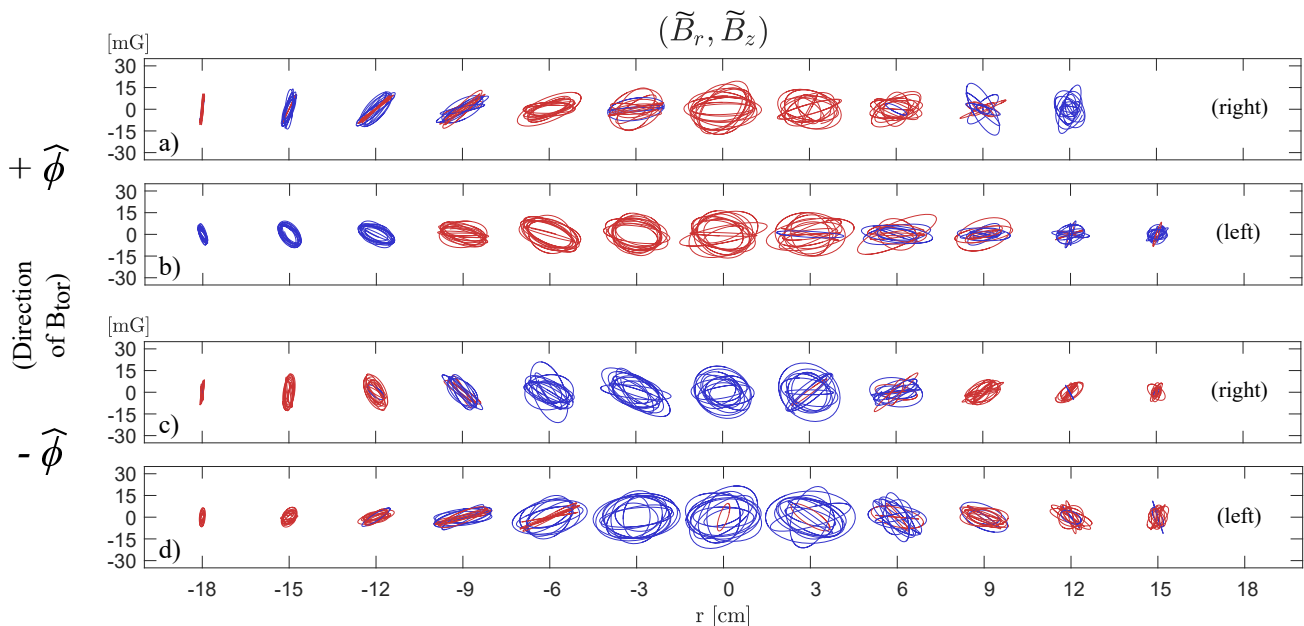


FIG. 11. Poloidal components of helicon wave measured with the B-dot along  $r$ , at  $z = 0$  cm, on the right (a, c) and left (b, d) of the BCA, for  $B_{tor}$  along  $\hat{\phi}$  (a, b) or along  $-\hat{\phi}$  (c, d). Red corresponds to a positive polarization of the wave with respect to the toroidal axis  $\hat{\phi}$  (see Fig. 9 (d)), blue to a negative one. Ten times are shown. See text for details.

respectively left and right from the BCA, with 10 different times equally spaced over the 1 ms measurements. Note that for visualization purposes, here the polarization is given with respect to the toroidal axis: red and blue respectively indicate a positive and negative polarization with respect to  $\hat{\phi}$ . The local polarization of the helicon wave is positive in the central plasma region and negative at the edges. This global pattern of polarization points to a helicon mode  $m = +1$ , as indicated by the simple modelling of helicon modes in a uniform cylindrical plasma<sup>36</sup>. Note however that since the latter modeling does not take into account density gradients nor toroidicity, which might have important effects on the wave, a more accurate modelling and comparison to experimental data is still required to identify the helicon modes launched in TORPEX with confidence. We note, finally, that the polarization pattern is almost identical on both sides of the BCA (Fig. 11 (a) and (b)), indicating that the helicon wave launched by the BCA is able to propagate throughout the whole toroidal vessel.

To check the robustness of these first measurements, the direction of the toroidal field is reversed, with  $\vec{B}_{tor} = -B_{tor}\hat{\phi}$ . The radial profiles of the mean amplitude of  $(|\vec{B}_r|, |\vec{B}_\phi|, |\vec{B}_z|)$  measured at the left and right of the BCA are shown Fig. 11 (c) and (d) respectively. As expected the levels of mean amplitude and fluctuations of  $|\vec{B}|$ , as well as the corresponding levels of mean amplitude between the components of  $|\vec{B}|$ , are similar to those measured with  $\vec{B}_{tor} = B_{tor}\hat{\phi}$  (Fig. 11 (a), (b)).

The magnetic configurations with  $\vec{B}_{tor}$  along  $\hat{\phi}$  and  $-\hat{\phi}$  are symmetric with respect to the toroidal direction. One could therefore expect a strong similarity between, on the one hand, the profiles measured on the right of the BCA with  $\vec{B}_{tor}$  along  $\hat{\phi}$  (Fig. 10 (b)) and the profiles measured on the left of the BCA with  $\vec{B}_{tor}$  along  $-\hat{\phi}$  (Fig. 10 (c)) and, on the other hand,

between the profiles in Fig. 10 (a) and (d). But since the BCA input frequency of 13.56 MHz falls by  $\sim 1$  MHz away from the BCA resonance, the BCA electromagnetic excitation might not be perfectly symmetric with respect to the axis  $\hat{r}$ . This is likely to explain the slight discrepancy observed between the pairs of profiles mentioned above.

As for the polarization of the helicon wave, it reverses with the direction of  $\vec{B}_{tor}$  as shown in Fig 11 (c) and (d). The mode polarization, with respect to the external magnetic field, is therefore identical in both cases  $\vec{B}_{tor} = +B_{tor}\hat{\phi}$  and  $\vec{B}_{tor} = -B_{tor}\hat{\phi}$ . This gives us further confidence in the ability of the BCA to launch and sustain a  $m = +1$  helicon mode in the whole torus of TORPEX.

## V. PLASMA GENERATION BY THE BIRDCAGE ANTENNA

We also explore the ability of the BCA to generate plasma with and without a magnetron-generated background plasma. The magnetron power  $P_{MAG}$  and BCA power  $P_{BC}$  are varied in  $\{0, 300, 600, 1000\}$  W. Hydrogen and argon SMT plasmas are explored, in the range of pressures  $p_0 \in \{0.1, 0.5, 1\} \times 10^{-3}$  mbar. The density is measured using a Langmuir probe at a position ( $r = -8$  cm,  $z = 0$  cm) where the magnetron plasma density is known to be the highest from previous studies (not shown), and at the toroidal location opposite to the BCA center ( $\phi \approx +180^\circ$ ) i.e. where the BCA generated plasma is expected to be weakest.

Figures 12 (a) and (b) show results for hydrogen and argon, respectively, at a pressure of  $0.1 \times 10^{-3}$  mbar. (We note that with hydrogen and a magnetron power of  $P_{MAG} = 1$  kW,



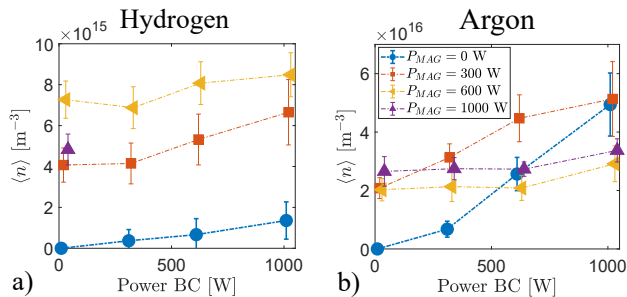


FIG. 12. Plasma density measured with Langmuir probe at ( $r = -8$  cm,  $z = 0$  cm,  $\phi \sim \pi$ ), for  $P_{MAG}$  and  $P_{BC} \in \{0, 300, 600, 1000\}$  W, at a pressure  $p_0 \sim 0.1 \times 10^{-3}$  mbar, in hydrogen (a) and argon (b).

switching on the BCA RF fields causes disturbances to the turbopumps, which prevented the corresponding plasma density measurements. This issue is expected to be solved in the near future by a Faraday shielding of the turbopump entries.) When the magnetron is on, the plasma density reaches  $n_e \approx 4 - 8 \times 10^{15} \text{ m}^{-3}$  in hydrogen, and  $n_e \approx 2 - 5 \times 10^{16} \text{ m}^{-3}$  in argon, as shown in Fig. 12 for  $P_{MAG} = [300; 600; 1000]$  W with the red, yellow and purple curves respectively. The BCA has a moderate impact on the magnetron-generated plasma with  $P_{MAG} = 600$  W and  $P_{MAG} = 1000$  W. Indeed with an equal amount of power fed to the BCA than delivered by the magnetron ( $P_{BC} = 600$  W and  $P_{BC} = 1000$  W respectively), the density increase stays lower than  $\sim 25$  %. However at a lower magnetron power of  $P_{MAG} = 300$  W and in argon, the plasma density increase from the BCA already reaches  $\sim 50$  % at  $P_{BC} = 300$  W, and up to  $\sim 150$  % at  $P_{BC} = 1000$  W. Finally with the magnetron switched off, the BCA is still able to generate substantial plasma density with respect to the magnetron-generated levels, with  $n_e \sim 1.5 \times 10^{15} \text{ m}^{-3}$  in hydrogen and  $n_e \sim 5 \times 10^{16} \text{ m}^{-3}$  in argon, at  $P_{BC} = 1000$  W. Note that the BCA is more efficient in argon, which is expected considering in hydrogen the power that is lost into vibrational and rotational energy level excitation, and which does not contribute to ionization.

Plasma density measurements with the BCA alone and with varying pressure are presented in Fig. 13. The plasma density increases with the BCA power  $P_{BC}$ , and with argon compared to hydrogen, which extends the observation in Fig. 12 to all pressures  $p_0 \in [0.1; 5; 1] \times 10^{-3}$  mbar. An increase of pressure is expected to cause a stronger damping of the helicon waves. Since these density measurements are done opposite to the BCA in the chamber, i.e. at a distance  $\sim 3$  m from the BCA, we could expect at this location a trend of plasma density decrease with pressure. Interestingly this trend is only clearly observed in Argon, and for  $P_{BC} \geq 600$  W. Globally, the plasma density does not vary significantly when the pressure is increased, staying within a factor 2 – 5 from the plasma densities at  $p_0 = 0.1 \times 10^{-3}$  mbar.

Note that these power and pressure scans were performed with the Langmuir probe at a single position. Therefore these measurements only provide a first broad overview of the ability of the BCA to generate plasma with or without the additional contribution of magnetron-generated microwaves.

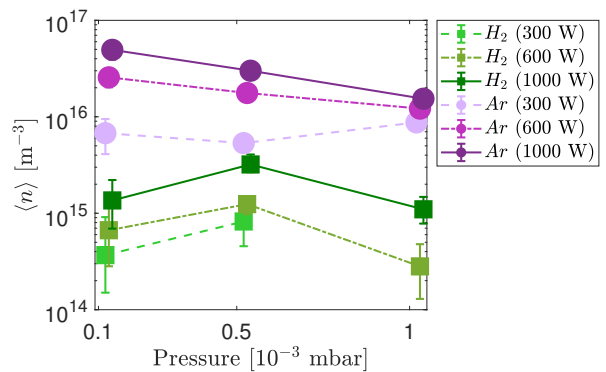


FIG. 13. Plasma density measured with Langmuir probe at ( $r = -8$  cm,  $z = 0$  cm,  $\phi \sim \pi$ ) as a function of pressure, for hydrogen and argon, without magnetron and for  $P_{BC} \in \{300, 600, 1000\}$  W.

Since the plasma density and potential shapes vary in 3D when the BCA is used, a deeper understanding of the impact of the BCA on plasma ionization in TORPEX needs spatially resolved measurements, with radial profiles such as the ones shown in Fig. 8 or even 2D measurements in  $(r, z)$ , at various toroidal locations, that will be the subject of future work.

## VI. CONCLUSIONS AND OUTLOOK

A 32.5 cm diameter helicon antenna has been designed, installed and successfully commissioned on the toroidal device TORPEX. An alternative design to the most commonly used half-helical antenna design was chosen, consisting in a resonant network of inductive legs connected in parallel by capacitors. This so-called birdcage antenna has the advantage of operating with low input voltage and current, making it easily scalable to larger dimensions than the  $\sim 10$  cm diameter sources typically used in low temperature plasma linear devices. The sinusoidal distribution of currents in the legs at resonance excites transverse  $m = 1$  magnetic field, making the BCA an efficient helicon source. The large surface coverage of the legs around the dielectric tube also makes this antenna efficient at generating and inductively coupling to the plasma, even at a (low) pressure of  $0.1 \times 10^{-3}$  mbar both in argon and in hydrogen. Finally, owing to an input inductance  $Z$  with  $\text{Re}(Z) \sim 100 \Omega$  and  $|\text{Im}(Z)| \lesssim 50 \Omega$  close to the resonance and in the presence of plasma, the matching of the BCA is straightforward and was easily achieved with a type T matching-box.

We stress that for all the measurements presented in sections IV and V, no adjustment to the BCA was needed. Once built and installed in TORPEX the BCA could be used without any further modification or RF coupling issues. This simplicity of use (once passed the design and building phases) summarizes the essential benefits brought by the BCA on a large scale set-up such as TORPEX.

Helicon waves are launched and sustained around the entire toroidal vessel of TORPEX, as demonstrated by B-dot measurements on both sides of the BCA. The wave polariza-

tion pattern suggests that a mode  $m = +1$  is dominant, by comparing our measurements to the simple modelling of helicon modes in a uniform cylindrical plasma. Further measurements and comparisons with models are required to confirm this mode identification. These will include measurements of the 2D profiles of the helicon wave amplitude across the poloidal cross section of TORPEX, as well as measurements of the toroidal wave number.

More generally, thanks to its numerous available diagnostics<sup>28,37,38</sup>, wide set of coils, and newly installed BCA, TORPEX is now a flexible and insightful test bed for the experimental study of the fundamental properties of helicon waves in toroidal geometry.

At a low power of 200 W, the BCA is shown to be able to launch helicon waves in a pre-existing argon plasma of density  $n_e \sim 10^{15} - 10^{16} \text{ m}^{-3}$ , without leading to modifications of the plasma density profile. This is an interesting feature for future studies in TORPEX, in which we plan to investigate the impact of resonant perturbations from helicon waves on the propagation of fast ions in a background turbulent plasma.

At powers up to 1 kW, plasma density measurements demonstrate the ability of the BCA to substantially modify the plasma equilibrium, as well as to generate, without contributions from the magnetron, a plasma density up to  $5 \times 10^{16} \text{ m}^{-3}$ .

The constraint imposed by the magnetron on the allowed values of magnetic fields (see Sec. I) is therefore removed. This opens the possibility to extend former studies carried out in TORPEX, such as blob transport mechanisms, with the added perspective of a varying magnetic field. The BCA moreover opens the way to entirely new experimental studies on TORPEX, such as transition to turbulence, or the impact of the magnetic field to the transport properties of fast ions. Comparing experiments with simulations as a mean for code validation will also now be possible in regimes previously inaccessible in TORPEX.

## ACKNOWLEDGEMENTS

This work has been carried out within the framework of the EUROfusion Consortium, via the Euratom Research and Training Programme (Grant Agreement No 101052200 — EUROfusion) and funded by the Swiss State Secretariat for Education, Research and Innovation (SERI). Views and opinions expressed are however those of the author(s) only and do not necessarily reflect those of the European Union, the European Commission, or SERI. Neither the European Union nor the European Commission nor SERI can be held responsible for them. This work was also supported in part by the Swiss National Science Foundation.

## Appendix A: B-dot calibration

Let us consider magnetic field fluctuations ( $B_x(t)$ ,  $B_y(t)$ ,  $B_z(t)$ ) at the location of the B-dot probe. The magnetic field  $B_x(t)$  mainly induces a voltage at the terminals of the B-dot

X-coil; this signal is denoted  $\varepsilon_{XX}(t)$ . However, since the coil orientation is not perfect, the measured signal at the X coil terminal might also be due to induced voltages from the  $B_y(t)$  and  $B_z(t)$  components, voltages respectively denoted  $\varepsilon_{XY}(t)$  and  $\varepsilon_{XZ}(t)$ . We can write:

$$V_x(t) = \varepsilon_{XX}(t) + \varepsilon_{XY}(t) + \varepsilon_{XZ}(t).$$

A similar statement holds for measured signals  $V_y(t)$  and  $V_z(t)$ . Then each voltage  $\varepsilon_{ij}(t)$ , induced in coil  $i$  by the magnetic field component  $j$  can be written as  $\varepsilon_{ij}(t) = f_{ij}(B_j(t))$ , with  $f_{ij}$  a function changing the amplitude and phase of each  $B_j(t)$  frequency components, respectively by a factor  $a_{ij}(\omega)$  and a phase  $\phi_{ij}(\omega)$ . This results in the following set of equations :

$$\begin{cases} V_x(t) = f_{XX}(B_x(t)) + f_{XY}(B_y(t)) + f_{XZ}(B_z(t)) \\ V_y(t) = f_{YX}(B_x(t)) + f_{YY}(B_y(t)) + f_{YZ}(B_z(t)) \\ V_z(t) = f_{ZX}(B_x(t)) + f_{ZY}(B_y(t)) + f_{ZZ}(B_z(t)) \end{cases} \quad (\text{A1})$$

Going to the spectral domain, and looking only at the components along a given frequency  $\omega_0$ , Eq. (A1) become

$$\begin{pmatrix} \hat{V}_x \\ \hat{V}_y \\ \hat{V}_z \end{pmatrix} = \underbrace{\begin{pmatrix} a_{XX}e^{i\phi_{XX}} & a_{XY}e^{i\phi_{YX}} & a_{XZ}e^{i\phi_{ZX}} \\ a_{YX}e^{i\phi_{XY}} & a_{YY}e^{i\phi_{YY}} & a_{YZ}e^{i\phi_{ZY}} \\ a_{ZX}e^{i\phi_{XZ}} & a_{ZY}e^{i\phi_{YZ}} & a_{ZZ}e^{i\phi_{ZZ}} \end{pmatrix}}_M \begin{pmatrix} \hat{B}_x \\ \hat{B}_y \\ \hat{B}_z \end{pmatrix}.$$

To determine the coefficients of the matrix  $M$ , the B-dot signal is measured for magnetic fields aligned along one direction  $x$ ,  $y$ ,  $z$ . For instance, along  $x$ ,

$$\begin{pmatrix} \hat{V}_{xx}^0 \\ \hat{V}_{xy}^0 \\ \hat{V}_{xz}^0 \end{pmatrix} = \begin{pmatrix} a_{XX}e^{i\phi_{XX}} & a_{XY}e^{i\phi_{YX}} & a_{XZ}e^{i\phi_{ZX}} \\ a_{YX}e^{i\phi_{XY}} & a_{YY}e^{i\phi_{YY}} & a_{YZ}e^{i\phi_{ZY}} \\ a_{ZX}e^{i\phi_{XZ}} & a_{ZY}e^{i\phi_{YZ}} & a_{ZZ}e^{i\phi_{ZZ}} \end{pmatrix} \begin{pmatrix} \hat{B}_0 \\ 0 \\ 0 \end{pmatrix} \quad (\text{A2})$$

$$= \begin{pmatrix} a_{XX}e^{i\phi_{XX}} \hat{B}_0 \\ a_{XY}e^{i\phi_{YX}} \hat{B}_0 \\ a_{XZ}e^{i\phi_{ZX}} \hat{B}_0 \end{pmatrix}. \quad (\text{A3})$$

Then the signal measured by any magnetic field is given by

$$\begin{pmatrix} \hat{V}_x \\ \hat{V}_y \\ \hat{V}_z \end{pmatrix} = \frac{1}{|\hat{B}_0|} \begin{pmatrix} V_{XX}^0 e^{i\phi_{XX}} & V_{XY}^0 e^{i\phi_{YX}} & V_{XZ}^0 e^{i\phi_{ZX}} \\ V_{YX}^0 e^{i\phi_{XY}} & V_{YY}^0 e^{i\phi_{YY}} & V_{YZ}^0 e^{i\phi_{ZY}} \\ V_{ZX}^0 e^{i\phi_{XZ}} & V_{ZY}^0 e^{i\phi_{YZ}} & V_{ZZ}^0 e^{i\phi_{ZZ}} \end{pmatrix} \begin{pmatrix} \hat{B}_x \\ \hat{B}_y \\ \hat{B}_z \end{pmatrix}.$$

From this expression, we conclude :

$$\begin{pmatrix} \hat{B}_x \\ \hat{B}_y \\ \hat{B}_z \end{pmatrix} = |\hat{B}_0| \cdot A^{-1} \cdot \begin{pmatrix} \hat{V}_x \\ \hat{V}_y \\ \hat{V}_z \end{pmatrix}.$$

The calibration measurements illustrated by Eq. (A2) are performed using a 10 cm diameter dedicated birdcage antenna. After a B-dot measurement of  $(V_x, V_y, V_z)$ , each raw signal  $V_i$  is filtered around  $f_0 = 13.56 \pm 1 \text{ MHz}$  using Matlab bandpass filter with a default transition band steepness of 0.85. Note that the spectrum of the filtered signal (green curve in Fig. 9 (b)) strongly peaks at  $f_0$ , and falls by over 7 orders of

magnitude at  $f_0 \pm 0.5$  MHz. Inside this frequency range, the calibration can still be considered valid; away from this frequency range, the frequency amplitude of the filtered signal is negligible. The calibration procedure is therefore not only applied to the 13.56 MHz component, but to the full filtered signals: this allows most of the low frequency fluctuations of the original signals to be kept.

## Appendix B: Equation solved in COMSOL

The equations that are used in COMSOL simulations are derived here. We assume cold ions, and consider the electron momentum equation

$$m_e n_e \partial_t \vec{u}_e = -en_e \vec{E} - en_e \vec{u}_e \times \vec{B} - m_e n_e \nu \vec{u}_e$$

$$\frac{m_e}{n} \underbrace{(\nu + i\omega)}_{\gamma} \vec{u}_e = -\vec{E} - \vec{u}_e \times \vec{B}.$$

Neglecting the inertia of the ions, the electric current can be written like  $\vec{j} = -en_e \vec{u}_e$ . Using then  $\vec{u}_e = -\frac{\vec{j}}{en}$  with  $\vec{\omega}_c = e\vec{B}/m_e$ , the momentum equation reads

$$\gamma \vec{j} = \varepsilon_0 \omega_p^2 \vec{E} - \vec{j} \times \vec{\omega}_c. \quad (\text{B1})$$

We now perform the cross product of  $\times \vec{\omega}_c$  to Eq. (B1), then substitute in the left hand side the expression of  $\vec{j} \times \vec{\omega}_c$  given by Eq. (B1), and obtain

$$\gamma^2 \vec{j} - \gamma \varepsilon_0 \omega_p^2 \vec{E} = \varepsilon_0 \omega_p^2 \vec{E} \times \vec{\omega}_c - (\vec{j} \times \vec{\omega}_c) \times \vec{\omega}_c.$$

By noting that  $(\vec{j} \times \vec{\omega}_c) \times \vec{\omega}_c = -\omega_c^2 \vec{j}_\perp$  (the direction  $\parallel$  and  $\perp$  being defined with respect to  $\vec{B}$ ), this last expression can be rewritten like

$$\gamma^2 \vec{j} + \omega_c^2 \vec{j}_\perp = \varepsilon_0 \omega_p^2 (\gamma \vec{E} + \vec{E} \times \vec{\omega}_c),$$

which, for the simple case  $\vec{B} = B \vec{e}_z$ , hence with  $\vec{\omega}_c = \omega_c \vec{e}_z$ , yields

$$\begin{pmatrix} (\gamma^2 + \omega_c^2) j_x \\ (\gamma^2 + \omega_c^2) j_y \\ \gamma^2 j_z \end{pmatrix} = \varepsilon_0 \omega_p^2 \begin{pmatrix} \gamma & \omega_c & 0 \\ -\omega_c & \gamma & 0 \\ 0 & 0 & \gamma \end{pmatrix} \begin{pmatrix} E_x \\ E_y \\ E_z \end{pmatrix}$$

This result can be written like

$$\vec{j} = \boldsymbol{\sigma} \cdot \vec{E}.$$

with  $\boldsymbol{\sigma}$  as defined in subsection III B. Combining this result with Maxwell's equations then yields the final equation for  $\vec{E}$  provided in subsection III B.

<sup>1</sup>R. W. Boswell. Plasma production using a standing helicon wave. *Phys. Lett.*, 7:457, 1970.

<sup>2</sup>S. Shinohara. Helicon high-density plasma sources: physics and applications. *Advances in Physics X*, 3:1420424, 2018.

<sup>3</sup>S. C. Thakur. Formation of the blue core in argon helicon plasma. *IEEE Transactions on Plasma Science*, 43:2754, 2015.

<sup>4</sup>E. Scime, R. Hardin, C. Biloiu, A. M. Keese, and X. Sun. Flow, flow shear, and related profiles in helicon plasmas. *Phys. Plasmas*, 14:043505, 2007.

<sup>5</sup>H. Bohlin, A. Von Stechow, K. Rabbarnia, O. Grulke, and T. Klinger. Vineta ii: A linear magnetic reconnection experiment. *Rev. Sci. Instrum.*, 85:023501, 2014.

<sup>6</sup>I. Furno, R. Agnello, U. Fantz, A. Howling, R. Jacquier, C. Marini, G. Plyushchev, P. Guittienne, and A. Simonin. Helicon wave-generated plasmas for negative ion beams for fusion. *EPJ Web Conf.*, 03014:157, 2017.

<sup>7</sup>F. Brochard, D. Genève, S. Heurax, V. Bobkov, D. Del Sarto, E. Faudot, A. Ghizzo, E. Gravier, N. Lemoine, M. Lesur, N. Louis, J. Moritz, T. Reveillé, V. Rohde, U. Stroth, G. Urbanczyk, F. Volpe, and H. Zohm. Spektre, a linear radiofrequency device for investigating edge plasma physics. *49th EPS Conference on Plasma Physics*, 2023.

<sup>8</sup>Tianyuan Huang, Chenggang Jin, Yaowei Yu, Jiansheng Hu, Jianhua Yang, Fang Ding, Xiahua Chen, Peiyu Ji, Jiawei Qian, Jianjun Huang, Bin Yu, and Xuemei Wu. Helicon-wave-excited helium plasma performance and wall-conditioning study on east. *IEEE Transactions on Plasma Science*, 48:2878, 2020.

<sup>9</sup>V. L. Vdovin. Current generation by helicons and lower hybrid waves in modern tokamaks and reactors iter and demo. scenarios, modeling and antennae. *Plasma Physics Reports*, 39:95–119, 2013.

<sup>10</sup>R. Prater, C.P. Moeller, R. I. Pinsker, M. Porkolab, O. Meneghini, and V.L. Vdovin. Application of very high harmonic fast waves for off-axis current drive in the diii-d and fnsf-at tokamaks. *Nucl. Fusion*, 54:083024, 2014.

<sup>11</sup>C. Lau. Aorsa full wave calculations of helicon waves in diii-d and iter. *Nucl. Fusion*, 58:066004, 2018.

<sup>12</sup>J. Li, X. T. Ding, J. Q. Dong, and S. F. Liu. Helicon wave heating and current drive in toroidal plasmas. *Plasma Phys. Control. Fusion*, 62:095013, 2020.

<sup>13</sup>X. Wu, J. Li, J. Chen, G. Xu, J. Dong, Z. Wang, A. Sun, and W. Zhong. Parametric study of helicon wave current drive in cfetr. *Nucl. Fusion*, 63:106015, 2023.

<sup>14</sup>B. Van Compernelle, M.W. Brookman, C.P. Moeller, R.I. Pinsker, A.M. Garofalo, R. O'Neill, D. Geng, A. Nagy, J.P. Squire, K. Schultz, C. Pawley, D. Ponce, A.C. Torrezan, J. Lohr, B. Coriton, E. Hinson, R. Kalling, A. Marinoni, E.H.Martin, R. Nguyen, C.C. Petty, M. Porkolab, T.Raines, J. Ren, C.Rost, O. Schmitz, H. Torreblanca, H.Q. Wang, J. Watkins, and K. Zeller. The high-power helicon program at diii-d: gearing up for first experiments. *Nucl. Fusion*, 61:116034, 2021.

<sup>15</sup>H.H. Wi, S.J. Wang, J. Kim, and J.G. Kwak. Rf design of helical long-wire traveling wave antenna for helicon current drive in kstar. *Fusion Eng. Des.*, 195:113983, 2023.

<sup>16</sup>S. K. P. Tripathi, D. Bora, and M. Mishra. Rf breakdown by toroidal helicons. *Pramana Journal of Physics*, 56:551, 2001.

<sup>17</sup>O. Grulke, F. Greiner, T. Klinger, and A. Piel. Comparative experimental study of coherent structures in a simple magnetized torus. *Plasma Phys. Control. Fusion*, 43:525, 2001.

<sup>18</sup>Y. Sakawa, M. Ohshima, Y. Ohta, and T. Shoji. Production of high-density hydrogen plasmas by helicon waves in a simple torus. *Phys. Plasmas*, 11:311, 2004.

<sup>19</sup>B. C. Zhang, G. G. Borg, and B. D. Blackwell. Helicon wave excitation and propagation in a toroidal heliac: Experiment and theory. *Phys. Plasmas*, 2:803, 1995.

<sup>20</sup>Manash Kr. Paula and D. Bora. Helicon plasma production in a torus at very high frequency. *Phys. Plasmas*, 12:062510, 2005.

<sup>21</sup>M. K. Paul and D. Bora. Radial characterization of wave magnetic field components during helicon discharge in a small aspect ratio torus. *J. Plasma Physics*, 76:39–48, 2010.

<sup>22</sup>A. Fasoli, I. Furno, and P. Ricci. The role of basic plasmas studies in the quest for fusion power. *Nat. Phys.*, 15:872–875, 2019.

<sup>23</sup>M. Podestà, A. Fasoli, B. Labit, M. McGrath, S. H. Müller, and F. M. Poli. Plasma production by low-field side injection of electron cyclotron waves in a simple magnetized torus. *Plasma Phys. Control. Fusion*, 47:1989–2002, 2005.

<sup>24</sup>S. H. Müller, A. Fasoli, B. Labit, M. McGrath, M. Podestà, , and F.M. Poli. Effects of a vertical magnetic field on particle confinement in a magnetized plasma torus. *Phys. Rev. Lett.*, 93:165003, 2004.

<sup>25</sup>A. Fasoli, B. Labit, M. McGrath, S. H. Müller, G. Plyushchev, M. Podestà, and F. M. Poli. Electrostatic turbulence and transport in a simple magnetized plasma. *Phys. Plasmas*, 13:055902, 2006.

<sup>26</sup>M. A. Lieberman and A. J. Lichtenberg. *Principles of Plasma discharges*

- and materials processing. John Wiley and Sons, 2 edition, 2005.
- <sup>27</sup>I. Furno, C. Theiler, V. Chaboz, A. Fasoli, and J. Loizu. Pre-sheath density drop induced by ion-neutral friction along plasma blobs and implications for blob velocities. *Phys. Plasmas*, 21:012305, 2014.
- <sup>28</sup>C. Theiler, I. Furno, A. Kuenlin, Ph. Marmillod, , and A. Fasoli. Practical solutions for reliable triple probe measurements in magnetized plasmas. *Rev. Sci. Instrum.*, 82:013504, 2011.
- <sup>29</sup>D. G. Miljak and F. F. Chen. Helicon wave excitation with rotating antenna fields. *Plasma Sources Sci. Technol.*, 7:61–74, 1998.
- <sup>30</sup>I. Shesterikov, K. Crombe, A. Kostic, D. A. Sitnikov, M. Usoltceva, R. Ochoukov, S. Heuraux, J. Moritz, E. Faudot, F. Fischer, H. Faugel, H. Fünfgelder, G. Siegl, and J.-M. Noterdaeme. Ishtar: A test facility to study the interaction between rf wave and edge plasmas. *Rev. Sci. Instrum.*, 90:083506, 2019.
- <sup>31</sup>Ph. Guittienne, A. A. Howling, and Ch. Hollenstein. Analysis of resonant planar dissipative network antennas for rf inductively coupled plasma sources. *Plasma Sources Sci. Technol.*, 23:015006, 2014.
- <sup>32</sup>Ph. Guittienne, A. A. Howling, and I. Furno. Resonant network antennas for radio-frequency plasma sources: Theory, technology and applications. *Institute of Physics Publishing*, 2024.
- <sup>33</sup>COMSOL Multiphysics® v. 6.2. [www.comsol.com](http://www.comsol.com). COMSOL AB, Stockholm, Sweden.
- <sup>34</sup>Itikawa database. [www.lxcat.net](http://www.lxcat.net). retrieved on November 13, 2023.
- <sup>35</sup>L.C. Pitchford, L.L. Alves, K. Bartschat, S.F. Biagi, M.C. Bordage, I. Bray, C.E. Brion, M.J. Brunger, L. Campbell, A. Chachereau, B. Chaudhury, L. G. Christophorou, E. Carbone, N. A. Dyatko, C. M. Franck, D. V. Fursa, R. K. Gangwar, V. Guerra, P. Haefliger, G. J. M. Hagelaar, A. Hoesl, Y. Itikawa, I. V. Kochetov, R. P. McEachran, W. L. Morgan, A. P. Nartovich, V. Puech, M. Rabie, L. Sharma, R. Srivastava, A. D. Stauffer, J. Tennyson, J. de Urquijo, J. van Dijk, L. A. Viehland, M. C. Zammit, O. Zatsarinny, and S. Pancheshnyi. Lxcat: an open-access, web-based platform for data needed for modeling low temperature plasmas. *Plasma Process. Polym.*, 14:1600098, 2017.
- <sup>36</sup>F. F. Chen. Plasma ionization by helicon waves. *Plasma Phys. Control. Fusion*, 33:339, 1991.
- <sup>37</sup>M. Baquero-Ruiz F. Avino O. Chellai A. Fasoli I. Furno R. Jacquier F. Manke and S. Patrick. Dual langmuir-probe array for 3d plasma studies in torpex. *Rev. Sci. Instrum.*, 87:113504, 2016.
- <sup>38</sup>F. Manke. *Fast ion transport phenomena in turbulent toroidal plasmas*. PhD thesis, École Polytechnique Fédérale de Lausanne, 2020.